

A FULL-SKY, HIGH-RESOLUTION ATLAS OF GALACTIC 12 MICRON DUST EMISSION WITH WISE

AARON M. MEISNER^{1,2} AND DOUGLAS P. FINKBEINER^{1,2}

Draft version March 27, 2018

ABSTRACT

We describe our custom processing of the entire Wide-field Infrared Survey Explorer (WISE) 12 μ m imaging data set, and present a high-resolution, full-sky map of diffuse Galactic dust emission that is free of compact sources and other contaminating artifacts. The principal distinctions between our resulting co-added images and the WISE Atlas stacks are our removal of compact sources, including their associated electronic and optical artifacts, and our preservation of spatial modes larger than 1.5 $^{\circ}$. We provide access to the resulting full-sky map via a set of 430 12.5 $^{\circ}$ ×12.5 $^{\circ}$ mosaics. These stacks have been smoothed to 15 $''$ resolution and are accompanied by corresponding coverage maps, artifact images, and bit-masks for point sources, resolved compact sources, and other defects. When combined appropriately with other mid-infrared and far-infrared data sets, we expect our WISE 12 μ m co-adds to form the basis for a full-sky dust extinction map with angular resolution several times better than Schlegel et al. (1998).

Subject headings:

1. INTRODUCTION

High-latitude complexes of resolved infrared sources were first identified by Low et al. (1984) using *IRAS* 60 μ m and 100 μ m observations (Wheelock et al. 1994). This so-called “infrared cirrus,” attributable to thermal emission from large dust grains in the interstellar medium, has since been probed in greater detail by a variety of instruments and detected over virtually the entire sky. Beginning in 1989, DIRBE mapped the full sky at ten infrared wavelengths from 1.25 μ m to 240 μ m with a reliable zero point, but inferior 0.7 $^{\circ}$ angular resolution (Boggess et al. 1992). Later, the ISO and IRTS missions (Kessler et al. 1996; Onaka et al. 1996; Tanaka et al. 1996) established that polycyclic aromatic hydrocarbons (PAHs) are responsible for the presence of cirrus at mid-IR wavelengths, displaying strong emission bands at 8.6 μ m, 11.3 μ m, and 12.6 μ m. Present day observatories are now capable of mapping the mid-IR and far-IR cirrus with excellent resolution and sensitivity. For example, *Herschel* has conducted pointed imaging observations from 70 μ m to 500 μ m with corresponding resolution ranging from 5.2 $''$ to 37 $''$ (Pilbratt et al. 2010). However, *Herschel* and *Spitzer* (Werner et al. 2004), each with field-of view \lesssim 5 $'$, only observed a very small fraction of the sky over their lifetimes.

On the other hand, the Wide-field Infrared Survey Explorer (WISE, Wright et al. 2010) has imaged the full sky in four broad infrared bandpasses at high angular resolution (Cutri et al. 2012). In the two bluest channels ($W1 = 3.4\mu\text{m}$, $W2 = 4.6\mu\text{m}$), the Rayleigh-Jeans tail of stellar emission dominates, with images displaying vast numbers of compact sources, and diffuse dust structure that is typically discernible only at very low Galactic latitudes. At the other end, the reddest band ($W4 = 22\mu\text{m}$) is strongly dominated by our Solar System’s interplanetary dust, its thermal emission peaking

between 15 μ m and 25 μ m. While the zodiacal foreground is still bright at $W3 = 12\mu\text{m}$, this bandpass was chosen to coincide with the strongest PAH emission features. As a result, Galactic cirrus is often prominent in $W3$, and has been imaged by WISE with high signal-to-noise over most of the sky in spite of bright zodiacal contamination that varies on large angular scales. Further, with a native resolution of 6.5 $''$, WISE $W3$ represents a dramatic improvement in angular resolution relative to previous mid-IR and far-IR full-sky data sets. This has motivated us to investigate WISE 12 μ m images as a way of mapping the diffuse mid-IR emission from Galactic interstellar dust and probing small-scale structure in the Milky Way ISM.

However, official WISE mission imaging data products do not include a clean map of the 12 μ m Galactic cirrus. To isolate diffuse $W3$ nebulosity, we have undertaken a custom per-exposure processing of the $W3$ data set and constructed custom stacks from these processed frames. In particular, we have:

- subtracted point sources and artifacts of bright point sources
- masked moving Solar System objects
- masked resolved compact sources
- eliminated single-epoch anomalies (e.g. satellite streaks and cosmic rays)
- corrected single-frame striping artifacts and per-quadrant offsets
- addressed time-dependent foregrounds due to the Moon and zodiacal light
- preserved large angular scale modes

Because PAHs trace the far-IR thermal emission from large grains, a particularly interesting application of diffuse $W3$ maps is the creation of high-resolution foreground templates and extinction estimates. In terms of predicting dust extinction, the industry standard is Schlegel et al. (1998, hereafter SFD), with 6.1 $'$ angular resolution limited by the asymmetric 4 $'$ *IRAS* beam. Even if we must smooth $W3$ considerably relative to its native resolution, we can still characterize the distribu-

¹ Department of Physics, Harvard University, 17 Oxford Street, Cambridge, MA 02138, USA; ameisner@fas.harvard.edu

² Harvard-Smithsonian Center for Astrophysics, 60 Garden St, Cambridge, MA 02138, USA; dfinkbeiner@cfa.harvard.edu

tion of interstellar dust over the full sky on angular scales many times smaller than the SFD/*IRAS* beam.

In §2 we summarize the relevant details of the WISE survey and its data products. In §3, we describe the point source catalog which enables us to model the PSF and perform PSF subtractions. In §4 we discuss our model of the PSF and related bright source artifacts. In §5 we describe our single-exposure processing pipeline that eliminates many contaminants of the diffuse *W3* emission. In §6 we discuss our custom stacks built from these processed single exposures. In §7 we discuss the full-sky map we are releasing³ and conclude in §8.

2. THE WISE DATA

2.1. WISE Survey Strategy

The WISE satellite followed a 95 minute, Sun-synchronous, polar orbit about Earth, always pointing close to zenith and imaging at nearly 90° Solar elongation. Over a single orbit, WISE scanned all ecliptic latitudes β at a particular ecliptic longitude λ , and then all β at longitude $(\lambda + 180^\circ)$. Successive 8.8 s, 0.8° frames overlap by $\sim 10\%$ in the scan direction, while corresponding frames in successive orbits have $\sim 90\%$ overlap.

Because the All-Sky Release spans just under seven months, the vast majority of the sky at low ecliptic latitude has a resulting integer coverage of 10-12. For our purpose of mapping diffuse emission, this substantial redundancy is useful in compensating for single-frame artifacts such as cosmic rays and satellite streaks. However, for typical locations on the sky, all 10-12 WISE epochs occur within a single ~ 20 hour time period. Unfortunately, the Moon and bright Solar System objects do not move far enough on this timescale to be rejected.

2.2. WISE Data Products

All WISE data products utilized throughout this work, including single exposures and catalogs, are drawn from the All-Sky Data Release (Cutri et al. 2012). The All-Sky Release features two distinct options for accessing WISE images. The ‘‘Atlas images’’ are a set of 18,240 co-adds, 1.5° on a side. While it might seem convenient for these co-adds to form the basis of our 12 μ m dust map, various considerations led us to conclude that we were best served by starting our analysis at the single-exposure level, then assembling our own custom stacks. First, each Atlas co-add is designed only to minimize the appearance of exposure boundaries within its footprint, but will not necessarily agree with its neighboring Atlas tiles on their overlaps. Additionally, the Atlas images contain all compact sources observed by WISE, which require extremely careful PSF subtraction in order to isolate the diffuse cirrus. The Atlas PSF must be defined in a complex way and would be difficult both to model and apply, given the multiple epochs combined at each Atlas pixel and the fact that the Atlas images have been smoothed.

Because of these Atlas co-add considerations, we have instead obtained WISE imaging data by downloading all ~ 1.5 million *W3* exposure sets, including the ‘‘intensity’’, ‘‘mask’’, and ‘‘uncertainty’’ files. The single exposures are referred to as ‘‘Level 1b’’ (L1b) images, are archived

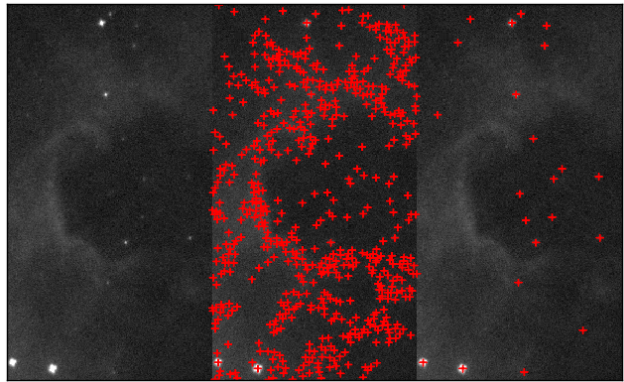


FIG. 1.— $0.15^\circ \times 0.28^\circ$ sub-region of a *W3* L1b image, centered at $(l, b) = (212.5^\circ, -0.45^\circ)$. Left: L1b data. Center: All-Sky Catalog, all nominal *W3* detections. Right: list of pointlike sources based on the COG cuts of §3.1.

by the NEOWISE project (Mainzer et al. 2011), and are the lowest-level publicly available WISE imaging data. L1b images are square, 1016 pixels on a side, and have a platescale of 2.75''/pixel. The x (y) axis of each L1b exposure is oriented perpendicular (antiparallel) to the scan direction.

To remove compact sources, we also make use of the WISE All-sky Source Catalog (§3) and WISE All-Sky Known Solar System Object Possible Association List (§5.3).

2.3. L1b Metadata Cuts

We discard a small subset of L1b exposures which, based on metadata alone, we know in advance will not be worthy of further processing. Our cuts generally follow the recommendations and cautions of Cutri et al. (2012). Specifically, we reject frames with `saa_sep` $\leq -5^\circ$, or `moon_sep` $\leq 12^\circ$, or `w3msknumsat` $> 500,000$ pixels, or with `dtanneal` $\leq 1,000$ s at high ecliptic latitude. These cuts remove 4.9% of the L1b images.

3. POINT SOURCES

A major goal of our L1b processing is the PSF subtraction of each pointlike source from every exposure in which it appears, along with correction of the artifacts associated with bright sources. In order to model the PSF and artifacts, and eventually to subtract appropriately centered/rescaled PSFs, we require a point source catalog. We opted not to build a custom point source catalog from scratch. Rather, we make use of the source positions and fluxes from the WISE All-Sky Source Catalog, only considering those sources with `w3snr` > 2 (Cutri et al. 2012).

However, cutting only on `w3snr` > 2 did not yield a satisfactory catalog. In the following subsections, we describe the additional cuts and custom augmentations we have made in order to obtain a catalog that best subtracts pointlike sources while preserving diffuse nebulousity. In particular, we were forced to address issues with very faint and very bright sources; at intermediate fluxes, we found the WISE All-Sky Source Catalog extremely reliable.

3.1. Nebula Fragment Rejection

³ See <http://wise.skymaps.info>.

The WISE All-sky Source Catalog was engineered to emphasize completeness over purity. Consequently, a striking feature of the $W3$ -detected sample ($w3snr > 2$) is the tendency for multitudes of dubious, faint sources to trace any sufficiently bright, filamentary dust structure (see Figure 1). Leaving this issue unaddressed, the filaments in PSF-subtracted images take on a distinctly “chewed up” appearance, compromising our estimate of the dust cirrus.

We were unable to identify any trivial cuts on e.g. signal-to-noise or source color that rectified this problem. However, we observed that the sources clustered on filaments tend to have a curve of growth (COG) more similar to that of a constant surface brightness profile than that of a PSF (see Figure 2). We measured the COG via a series of aperture magnitudes, $w3mag_n$, for $n = 1, \dots, 6$, available in the All-Sky Catalog. The PSF COG was computed by integrating our model from §4 in the relevant apertures. We were able to satisfactorily reject nebula fragments by cutting those sources with COG more consistent with constant surface brightness than with the $W3$ PSF model. We also discarded sources with an undefined error $w3sigm_1$ on their innermost aperture magnitude, $w3mag_1$. The PSF versus constant surface brightness comparison was calculated in the sense of minimum absolute deviation, as the majority of All-Sky Catalog errorbars ($w3sigm_n$) were undefined for the faint sources of interest, precluding a formal likelihood analysis.

The objects thus removed constituted a non-negligible fraction of All-Sky Catalog sources with $w3snr > 2$. Prior to the COG cut, the All-Sky Catalog contained ~ 167 million sources detected in $W3$; applying the COG filter reduced the number of remaining $W3$ sources to ~ 41 million.

3.2. Custom Bright Source Fluxes

By employing our detailed model of the PSF wings (see §4), we were able to derive custom bright source parameters that yielded cosmetically optimal PSF subtractions. Our procedure ignores the saturated core of each bright source, fitting only an annulus containing the wings.

Specifically, we fit custom fluxes for those $\sim 15k$ sources in the All-Sky Source Catalog brighter than $w3mpro = 2$ (>5 Jy). This threshold has no special significance with regard to the WISE instrumentation, and its choice is driven by pragmatic concerns relating to e.g. our available computational resources. To fit each bright source, we consider an annulus about its centroid with outer radius $2.1'$. The inner boundary of the annulus was determined via a flood-fill of pixels near saturation ($>20,000$ DN), starting from the centermost pixel. After dilating this saturation mask by 3 L1b pixels, we excluded the resulting interior region from the flux fit. We then perform a linear least squares fit to the annulus pixel values. The model is the sum of a rescaled PSF and a constant offset representing the background level. Thus, there are two parameters: the background offset and PSF rescaling factor, from which we infer the source flux. For each source, such a fit is performed for each L1b image in which the entire fitting annulus falls within the image boundaries. The L1b pixels of each fit are inverse variance weighted based on the corresponding L1b uncertainty image. The flux assigned is taken to be the

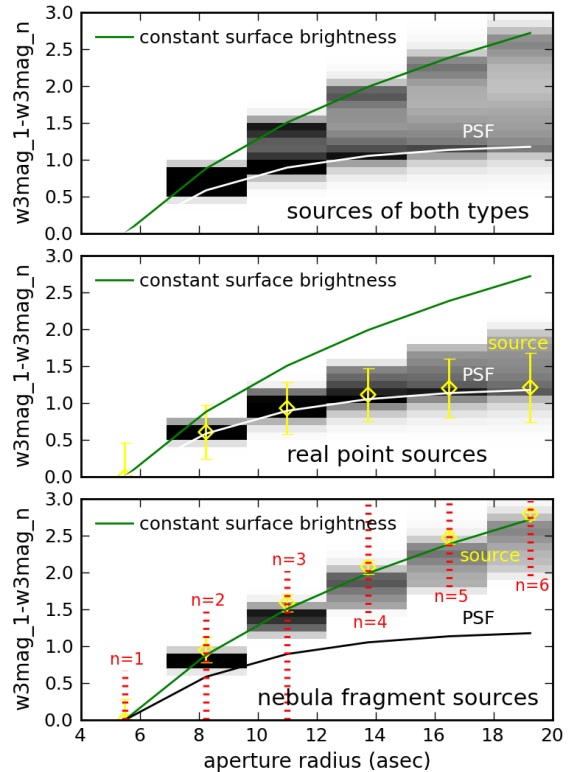


FIG. 2.— Top: $W3$ aperture 1 minus $W3$ aperture n vs. radius for a set of $\sim 250,000$ All-sky Catalog sources (grayscale), along with the expected curve for a PSF (white line) and constant surface brightness (green line). Middle: same for sources classified as true point sources by our COG cut, with an example such source shown (yellow). Bottom: same, but for sources classified as nebula fragments by our COG cut, along with an example such source (yellow).

median of the individual L1b fluxes. Typically 9 L1b fits per source are performed.

We also computed custom centroids for bright sources in order to achieve cosmetically optimal PSF subtractions. After computing our custom fluxes, we recompute the centroid by fixing the background and flux, but fitting x, y offsets via Levenberg-Marquardt chi-squared minimization.

Figure 3 shows a representative sample of 25 bright sources drawn from ~ 300 square degrees of the sky which we processed in turn with the raw All-sky Catalog parameters and our custom parameters. On the whole, our custom parameters clearly provide substantial improvement in the monopole and dipole components of the residuals. For the purposes of this work, we only care about the cosmetic quality of our point source subtracted maps, and have therefore chosen bright source subtractions based on our custom parameters. We caution, however, that our custom bright source parameters have not been thoroughly vetted against other mid-infrared calibrators, whereas those of the official All-sky Source Catalog have been (Cutri et al. 2012).

4. POINT SPREAD FUNCTION

Because the space-based WISE mission did not have to contend with atmospheric effects, we expect its PSF to be rather stable, and that a detailed characterization will lead to excellent PSF subtractions. Figure 4 shows a

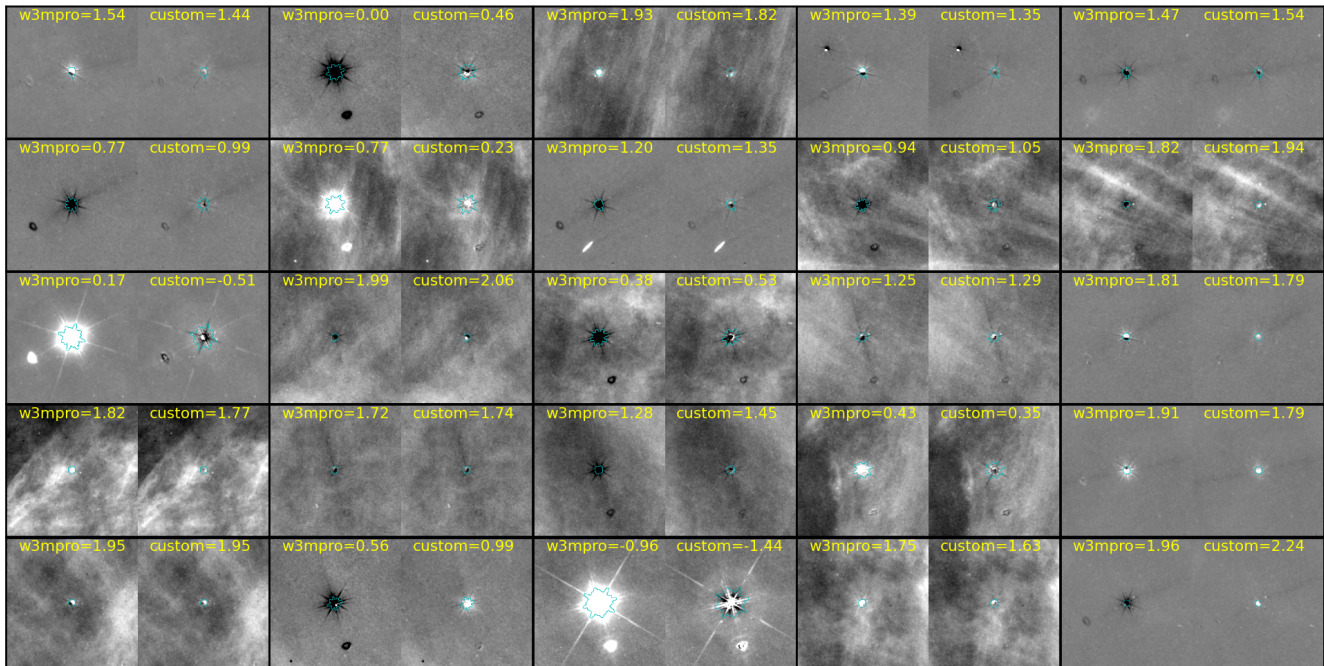


FIG. 3.— Comparison of bright source subtraction residuals using All-sky Source Catalog parameters versus our custom-fitted parameters. We have optimized the fit to subtract the PSF wings. Blue outlines indicate pixels flagged with our “bright region of point source profile” mask bit (see Table 2). The diffraction spikes and ghost also appear explicitly in the bit-mask.

schematic of our model for the imprint⁴ of a single bright point source in the *W3* data. The model includes some features common to astronomical imaging: a bright PSF core, faint but extensive wings, and diffraction spikes. Additionally, appearing within the same exposure as the bright source itself, a doughnut-like optical “ghost” results from the WISE optics. This ghost is offset $9.5'$ in the scan direction relative to the source centroid. When a source is bright enough to saturate in its core, the following exposure one frame cycle later displays a saucer-like electronic defect termed the “first latent”. Another frame cycle after that (two exposures following the bright source detection) the electronics are still recovering and a fainter “second latent” is observed. For further details about these effects, see the Explanatory Supplement (Cutri et al. 2012). In the following subsections we describe our models for each of these features, which we later use to PSF subtract pointlike objects and correct bright source artifacts.

Our PSF modeling was iterative; after creating an initial model for the PSF wings based on out-of-the-box fluxes from the All-Sky Catalog, we used this model to fit custom bright source fluxes (§3.2). We then fed our refined fluxes back into the PSF/artifact modeling procedure. The models eventually used to create the stacks of §7 were all based on our custom bright source fluxes. Henceforth, the name *w3mag* will refer to our custom bright source fluxes, whereas *w3mpro* will refer specifically to values quoted directly from the All-Sky Catalog.

4.1. PSF Core

We cannot rely upon one single sample of WISE sources to model all portions of the *W3* PSF. For in-

stance, the extremely bright sources that have high signal-to-noise in their outer wings will be saturated in their cores, and thus useless in modeling the innermost several FWHM.

W3 sources begin to saturate in their very central pixels at $3.5 < w3mpro < 4.0$. In order to leverage the brightest non-saturated sources, we modeled the PSF’s inner $1.15'$ (10.6 FWHM, the “core”) using ~ 4600 All-Sky Catalog sources with $4 < w3mpro < 5$ and $|b| > 40^\circ$.

To fully reap the benefits of PSF subtraction at the single exposure level, our model must include spatial PSF variation across the chip, as a function of source centroid (x_c, y_c) . We begin by gathering cutouts from individual L1b images in which each source in our sample appears. These cutouts include those in which the PSF core is only partially contained within the image. This permits us to model the PSF variation all the way to the chip’s edges. Typically 10 such cutouts per source were collected. We sinc shift each cutout in both x and y directions by a fraction of a pixel such that all cutouts are precisely centered on the source centroid. Additionally, each L1b cutout is background subtracted and rescaled to an arbitrary common source flux. The (x_c, y_c) location of each cutout’s centroid within its original L1b image is also stored.

For each pixel location with respect to the PSF model centroid, the set of rescaled pixel values available from these cutouts is fit with a third order polynomial surface in (x_c, y_c) . We chose third order because our measurements of the PSF FWHM as a function of position in the chip revealed a dependence that required third order terms. The per-pixel fit is performed independent of other neighboring pixels and carried out via weighted linear least squares, including iterative outlier rejection. The weights are inverse variances based on propagation of errors from the L1b uncertainty masks. The result is

⁴ We use this term to refer to the PSF and additional non-linear after-effects in subsequent exposures.

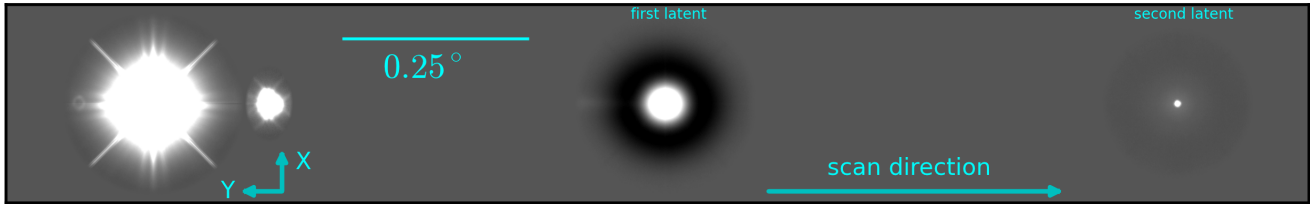


FIG. 4.— Our model for the imprint of a single bright point source, including PSF wings, core, ghost and first, second latents.

a polynomial model of the PSF core wherein the zeroth order term represents the PSF at the center of the chip, and higher order terms correct for PSF variation across the chip.

4.2. PSF Wings

Our procedure for modeling the PSF wings is quite similar to that employed in modeling the PSF core (§4.1). Our model for the PSF wings consists of a rectangular region $14.9'$ on a side, and thus characterizes the *W3* PSF behavior over a diameter of ~ 140 FWHM.

In assembling a sample of sources with which to model the PSF wings, we aimed to use approximately the $\sim 100^{\text{th}}$ - 1100^{th} brightest high-latitude sources on the sky. Specifically, our sample was defined to be those sources with $-2 < \text{w3mag} < 1$, and with $|b| > 15^\circ$. This sample contains 1046 unique sources. We found that the handful of $\text{w3mag} < -2$ sources were predisposed towards anomalous defects such as bleeding, and thus would contribute systematic problems to the PSF model despite having nominally high signal-to-noise in the wings.

We again collect cutouts as in §4.1, but model the per-pixel spatial variation with only first order terms in x_c , y_c . Higher order terms did not appear necessary and tended to destabilize the per-pixel polynomial fit in outer regions of the wings where signal-to-noise is low. The resulting model of the PSF core and wings, tapered according to §4.5, is shown on a logarithmic stretch in Figure 5. The diffraction spikes are not treated specially relative to other pixels in the model of the PSF wings.

4.3. Ghost

The optical ghost location with respect to the PSF core depends strongly on the centroid coordinates of its parent source, particularly x_c . As x_c ranges from one edge of the image to the other, $x_c \approx 0$ to $x_c \approx 1015$, the ghost centroid shifts in position relative to x_c by $0.5'$ (~ 11 L1b pixels). We initially attempted to model this translation of the ghost relative to x_c with an approach similar to that in §4.1, §4.2, employing high-order per-pixel polynomials. However, we found this model did not satisfactorily capture the ghost’s translation and became unstable for x_c near the L1b edges.

We thus resorted to a ghost model in which the ghost shape remains constant, but can translate with respect to x_c and can be amplified/suppressed by an overall rescaling factor f_g that varies with (x_c, y_c) . To create such a model, we again started by extracting many L1b cutouts. The same 1046 sources used to model the PSF wings were also used to model the ghost. We began by computing the centroid of the ghost in each cutout, and fit a second-order polynomial model to the ghost’s offset relative to

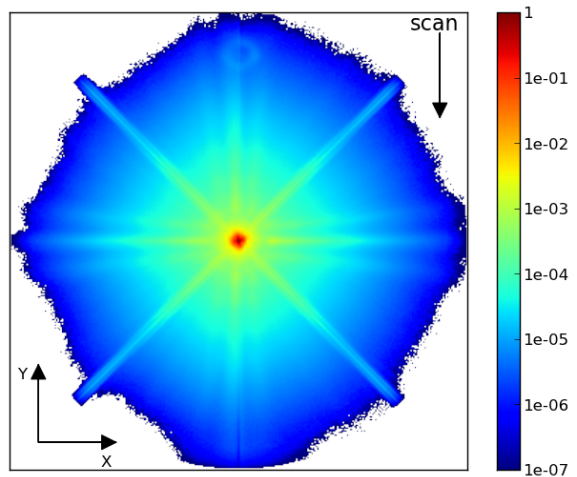


FIG. 5.— Our model of the *W3* PSF core and wings at chip center, on a logarithmic stretch, tapered according to §4.5. The image is $14.9'$ (325 L1b pixels) on a side. L1b x -axis, y -axis orientations, as well as the scan direction, are labeled with arrows.

(x_c, y_c) . We then used this ghost translation model to rectify all the cutouts to a common fiducial ghost centroid with respect to (x_c, y_c) . The rectified cutouts allowed us to compute the ghost profile via a weighted average with iterative outlier rejection. To determine f_g , we modeled each rectified cutout as a sum of an offset and f_g times the ghost profile. Finally, we fit a second-order polynomial in (x_c, y_c) to the set of f_g values we obtained. With $f_g = 1$ for (x_c, y_c) at the chip center, our resulting model always has $0.85 < f_g < 1.06$.

4.4. Latents

4.4.1. First Latent

The first latent always appears with the same centroid coordinates (x_c, y_c) as its parent bright source, but one exposure later. By “one exposure later” we do not necessarily mean an increment of one in the L1b `frame_num` parameter. Rather, we mean an exposure which follows the bright source detection by exactly one frame cycle, 11.1 s. There is not always such an exposure for every bright source detection.

We collect the relevant cutouts by identifying those frames that follow detection of sources with $-3 < \text{w3mag} < 1$, $|b| > 15^\circ$ by 11.1 s. There are 1088 such sources. Our latent model is built on a rectangular footprint, $14.9'$ on a side. To characterize the first latent shape, we assume the latent scales linearly with source flux, as do other PSF components. We then rescale our cutouts, and determine the latent profile via a weighted average with iterative outlier rejection.

In reality, the first latent does not scale linearly with parent source flux. As parent flux decreases, the first latent amplitude increases relative to the parent source flux (until the parent source no longer saturates, in which case no latent will arise). Our model accounts for this fact by assuming the latent shape to be independent of parent flux, but allowing for a scalar nonlinearity factor f_l that is a function of parent flux. f_l is defined to be a correction relative to perfect linear scaling, and would be identically unity if the latent behaved as a true component of the PSF, proportional in amplitude to parent source flux. We compute f_l by creating a first latent model in each bin of 0.2 mag and computing their relative amplitudes. A smooth model for f_l results from fitting a polynomial to these relative amplitudes. f_l varies between 0.38 and 1.25.

4.4.2. Second Latent

We similarly take the second latent to be an artifact appearing 22.2s after a bright source detection, with (x_c, y_c) identical to that of the parent source. The procedure for fitting the second latent profile is analogous to that for the first latent. To model the second latent we use those sources with $-3 < \mathbf{w3mag} < -0.5$ and $|b| > 15^\circ$. Our second latent model is rectangular, 12.4' on a side. Because the second latent appeared less strongly nonlinear and was more difficult to characterize in narrow bins of $\mathbf{w3mag}$ than the first latent, no nonlinearity correction was computed. We also found that higher-order latents were too faint to reliably model.

4.5. Tapering

Our models for the PSF wings and ghost, as well as the latents, are defined on rectangular footprints, and may not necessarily asymptote identically to zero precisely at their very edges. Thus, subtracting our rectangular models would introduce extra power in modes oriented parallel to the x, y axes of the chip. For this reason we taper the aforementioned models to zero before performing subtractions. This is achieved by premultiplying the models by weights that decline smoothly from unity in each model's center to zero at each model's boundary. We denote the angular extent of a particular model in the x (y) direction θ_x (θ_y). In order to define our tapering weight we first compute a radial coordinate r relative to the model's central pixel:

$$r = \sqrt{(\theta_y/\theta_x)^2 \Delta x^2 + \Delta y^2} \quad (1)$$

Where Δx and Δy are displacements relative to the model centroid. For $r \leq r_{in}$, the tapering weight is unity, and for $r \geq r_{out}$ the tapering weight is zero. For $r_{in} < r < r_{out}$, the weight transitions from 1 to 0 linearly with respect to r . Table 1 lists $\theta_x, \theta_y, r_{in}, r_{out}$ for the models that we taper prior to subtraction.

4.6. Relating Counts and Magnitudes

In order to relate magnitudes ($\mathbf{w3mag}$) to L1b counts (DN), we must accurately determine the ‘‘zero-point magnitude’’ m_0 , such that a source with integrated flux of 1 count corresponds to $\mathbf{w3mpro} = m_0$.

We chose to define our m_0 with respect to an aperture of diameter 1.8'. We then conducted aperture photome-

TABLE 1
MODEL SIZES & TAPERING PARAMETERS

| Model | θ_x | θ_y | r_{in} | r_{out} |
|--------------------|------------|------------|----------|-----------|
| PSF Wings (bright) | 14.9' | 14.9' | 6.7' | 7.4' |
| PSF Wings (faint) | 5.3' | 5.3' | 1.9' | 2.6' |
| Ghost | 6.2' | 4.0' | 1.7' | 2.0' |
| First Latent | 14.9' | 14.9' | 6.7' | 7.4' |
| Second Latent | 12.4' | 12.4' | 5.5' | 6.2' |

try on the same set of high-latitude, unsaturated, moderately bright sources used to model the PSF core. In order to determine m_0 , we performed a least-squares fit with iterative outlier rejection to the trend of $\mathbf{w3mpro}$ vs. $2.5 \log_{10}(F_{DN})$, F_{DN} signifying the total counts within the 1.8' aperture. The result determined $m_0 = 17.645$. Reassuringly, the best-fit slope was indeed very nearly unity. More generally, we found no evidence for significant nonlinearity of $\mathbf{w3mpro}$ for unsaturated sources at any point throughout this work.

We found that m_0 was sufficiently stable with time throughout the All-Sky Release portion of the WISE mission to be considered a constant. Similarly, we did not find any evidence for temporal variation of the PSF shape.

5. SINGLE EXPOSURE PIPELINE

We have built a single-exposure pipeline meant to remove and/or flag several contaminants affecting the diffuse $12\mu\text{m}$ emission we wish to isolate. Each of the ~ 1.5 million L1b exposures is processed independently. The pipeline attempts to remove all traces of pointlike sources by combining the All-Sky Catalog (including our custom bright fluxes and COG cuts) with our models of the PSF and related defects. SSOs are also interpolated over and flagged. Additional single-exposure mask bits are set, and propagate into extensions of the tile co-adds, as discussed in §7. The following subsections detail our L1b processing steps.

5.1. L1b Mask

Each raw L1b intensity image is accompanied by a corresponding `*-w3-msk-1b.fits` bit-mask provided by the WISE team. We will refer to such files as `msk` files, so as not to confuse them with our own custom L1b masks. The first step in our L1b processing is to create a mask of bad pixels in the raw L1b image which we must interpolate over, based on the `msk` file. We dilate the cosmic ray mask by a kernel of sidelength 3 pixels. Bad pixels are then taken to be those flagged in the dilated CR mask, or with any of the static bad pixel `msk` bits set, or with a NaN value. We immediately interpolate over this mask before proceeding.

5.2. Static Point Sources

Next we move on to correcting for static pointlike sources. From our custom catalog, we retrieve a list of all those sources whose PSF wings or ghost image, as represented by our models, have non-zero overlap with the L1b image at hand. This includes objects with centroids that fall outside the boundaries of the L1b image.

For each point source in the list, we compute its centroid coordinates (x_c, y_c) based on the L1b WCS and

create a PSF model including the core, wings and ghost. The core and wings are computed from the per-pixel polynomials in (x_c, y_c) described in §4.1, §4.2. The ghost image is derived based on the model of §4.3, taking (x_c, y_c) into account through the ghost centroid translation and the amplification factor f_g . When computing these models, we always bound x_c, y_c to lie within the image, so as to not extrapolate beyond the limitations of our various polynomial corrections in x_c, y_c . We renormalize the PSF according to each source’s **w3mag** value and the prescription of §4.6.

Before finally subtracting this PSF model from the L1b image, two further steps are taken: (1) we sinc shift appropriately such that the observed and model source centroids match at the sub-pixel level (2) we apply the tapering prescription of §4.5 so as not to introduce rectangular boundaries into the model-subtracted images. These two steps are also applied before subtracting the first and second latent models as described in §5.2.1, §5.2.2 below.

It was not necessary to apply the full 14.9’ model of the PSF wings to arbitrarily faint sources. Rather, for sources deemed faint, we subtracted a 5.3’ cutout of the PSF core/wings. This smaller model does not include the ghost. We set the threshold distinguishing bright versus faint at **w3mag** = 4.2 for typical coverage, though the exact cutoff was scaled on a source-by-source basis to account for coverage **w3m**.

For sufficiently bright sources, the innermost pixels of the PSF subtraction tended to show strong residuals. Consequently, we interpolate over such regions, using a circular mask of size that varies with **w3mag**. Such interpolation only occurs for sources with **w3mpro** \leq 9. We flagged pixels interpolated over in this manner with bit 4 of our mask. These interpolations affect a very small fraction, <0.25%, of the sky.

Based on the appropriately shaped and scaled PSF model derived for each source, a corresponding bit-mask is created. Saturated pixels within the PSF core (>30,000 DN) are flagged with bit 0. Bright regions of the PSF profile (>250 DN) are flagged with bit 2. Pixels within the ghost model that have values greater than 10^{-4} times the peak value of the PSF core are flagged with bit 1. This mask bit is meant to trace the general outline of the entire ghost model. Especially bright pixels within the ghost model (>20 DN) are flagged with bit 5.

5.2.1. First Latent

The presence of a first latent in a given L1b frame indicates that a bright source at the latent’s (x_c, y_c) location was observed in a frame 11.1 s prior. For each L1b frame, we attempt to identify the frame 11.1 s prior to it. If no such frame exists, then no first latent corrections are made. If such a frame exists, we obtain a list of point sources bright enough to induce a first latent that were observed within the prior frame. The threshold for inducing a latent is **w3mag** < 4. An appropriately rescaled latent model, taking into account the nonlinearity correction f_i , is then subtracted at the location of each bright source in the prior exposure. The first latent flag (bit 3, see Table 2) is set for pixels within a diameter of 9 pixels relative to each first latent centroid.

5.2.2. Second Latent

TABLE 2
BIT-MASK SUMMARY

| Bit | Description |
|-----|--|
| 0 | saturated point source core |
| 1 | point source ghost |
| 2 | bright region of point source profile |
| 3 | first latent of point source |
| 4 | PSF subtraction residual interpolated over |
| 5 | bright region of point source ghost |
| 6 | SSO interpolation |
| 7 | resolved compact source |
| 8 | second latent of point source |
| 9 | third latent of point source |
| 10 | fourth latent of point source |
| 11 | bright SSO ghost |
| 12 | bright SSO latent |
| 13 | point source diffraction spike |
| 14 | saturated pixel not in static mask |
| 15 | Moon contamination |
| 16 | RC3 optical galaxy |
| 17 | big object (M31, LMC, SMC) |
| 18 | Solar System planet |
| 19 | reference comparison failure |
| 20 | line-like defect |
| 21 | low integer frame coverage |
| 22 | ecliptic plane |

The procedure for correcting and flagging the second latent is virtually identical to that for correcting the first latent. The important distinction is that the relevant list of bright sources will correspond to the frame 22.2 s prior to the L1b image being processed, if such a prior frame exists. We set the threshold for second latent correction at **w3mag** < -0.5.

5.2.3. Third, Fourth Latents

As mentioned in §4.4.2, we only modeled the first and second latents. While we did not model the third and fourth latents, we do include mask bits to flag their locations (see Table 2). We carefully inspected the imprints of very bright sources in early versions of our stacks to determine which sources required mask bits to be set for third and fourth latents. We found that sources with **w3mag** < 0 required the third latent to be flagged, and those with **w3mag** < -1.5 required the fourth latent be flagged as well. Flagging the third (fourth) latent simply involved acquiring the source list for the frame 33.3 s (44.4 s) prior to the frame under consideration.

5.2.4. Diffraction Spike Mask

While the diffraction spikes were modeled simply as a part of the PSF wings, we judged that a special mask bit labeling potential diffraction spike residuals might be of value. Using our PSF model, we calibrated the angular extent over which diffraction spikes would be detected as a function of source flux and integer coverage, conservatively assuming all epochs to have identical scan direction and negligible background structure. The threshold for assigning a diffraction spike mask is **w3mag** < 4.25 for typical coverage.

We then computed two corrections to this simplistic model to handle relevant edge cases. The first problematic scenario arises near the ecliptic poles, where scans converge from many different directions and integer coverage is very high. Applying the naive model would result in excessively large, nearly circular diffraction spike

masks in our tile stacks at very high $|\beta|$. Consequently, we create an effective magnitude by adding to $w3mag$ a term that accounts for diffraction spike attenuation due to varying L1b exposure orientation. We then use this effective magnitude instead of $w3mag$ to compute the appropriate diffraction spike extent.

The second case is that of bright, highly structured background emission, e.g. in the Galactic plane. In such regions, the systematic variation and elevated Poisson noise of the background will diminish the angular extent over which diffraction spikes and their residuals are readily apparent. To quantify such background structure, we rely upon SFD *IRAS* $100\mu\text{m}$ (i100). We therefore computed \mathcal{R}_{100} , an $N_{side} = 64$ HEALPix map (Górski et al. 2005), wherein each $\sim 1^\circ$ pixel stores the RMS of the i100 values sampled at the $N_{side} = 512$ pixel centers nested within its boundaries. \mathcal{R}_{100} is typically of order 10^{-1} MJy/sr at high $|\beta|$, but can be of order 10^3 MJy/sr in bright regions like the Galactic center. A term logarithmic in \mathcal{R}_{100} was added to the effective magnitude we used to compute the appropriate diffraction spike mask extent for $\mathcal{R}_{100} > 3$ MJy/sr. This correction adequately reduced the diffraction spike extent in regions with substantial diffuse structure.

5.3. Solar System Objects

To some extent, the outlier rejection steps in our mosaicking process (§7) eliminate moving objects, without any special treatment of SSOs in particular. However, there are many cases in which moving objects proceed slowly enough so as to contaminate the same location on the celestial sphere at multiple epochs. Furthermore, the WISE team provides a convenient catalog of potential SSO detections – the WISE All-Sky Known Solar System Object Possible Association List (Cutri et al. 2012, henceforth PAL). For these reasons, we chose to incorporate steps for masking and flagging SSOs into our L1b processing pipeline.

The PAL uses the orbits of known SSOs to calculate the expected locations of these objects within each L1b exposure. If there exists a WISE detection of some source nearby to one of these predicted locations, the measured properties of that source will be recorded in the PAL. Importantly, each PAL entry contains an L1b frame identification, coordinates of the source within that L1b image, and the source’s profile-fit magnitude, again designated $w3mpro$. In some cases, the associations may be inertial sources, or spurious detections, as PAL entries are based on single-epoch photometry. For our purposes, sample purity is not of much concern. Even if we interpolate unnecessarily in some cases, the redundant WISE coverage will tend to render such a mistake imperceptible.

For each SSO in a given L1b exposure, we produce a mask centered about the SSO centroid that scales in size with the detected object’s brightness. These masks each contribute to bit 6 of our L1b bit-mask (see Table 2), which denotes the pixels we have interpolated over within the L1b image to remove the SSO core/wings. The mask about an SSO’s centroid consists predominantly of a circular region, with diameter varying from $0.3'$ (7 L1b pixels) for $w3mpro \geq 10$ to $3.5'$ (83 L1b pixels) for $w3mpro \leq 1.4$. In addition, we apply our diffraction spike model of §5.2.4 to SSOs with $w3mpro < 3$. We interpolate over these SSO diffraction spikes at the L1b level, and the af-

fected pixels are also flagged with bit 6. We considered PSF subtracting SSOs rather than simply interpolating over them, but found that the single-epoch PAL photometry was too unreliable and yielded a cosmetically inferior result.

In addition to addressing each SSO’s core, wings and diffraction spikes, we take further actions with regard to artifacts of very bright SSOs. For SSOs with $w3mpro < 2.5$, we mask and interpolate over an elliptical region surrounding the object’s ghost image. SSO ghost interpolation is registered in our bit-mask with bit 11. Similarly, for SSOs brighter than $w3mpro = 1$, we interpolate over the first latent and correspondingly set mask bit 12. Figure 6 provides an example of our SSO masking and interpolation results.

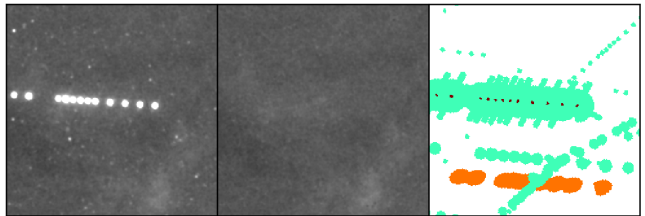


FIG. 6.— $0.4^\circ \times 0.4^\circ$ co-add cutout at $(l, b) = (355.68^\circ, 43.84^\circ)$, $(\lambda, \beta) = (226.74^\circ, 13.19^\circ)$, illustrating our SSO mask bits. Green, orange, and red represent bits 6, 11, and 14 respectively (see Table 2). The bright SSO (381 Myrrha) reveals the detailed nature of bit 6, which incorporates the diffraction spike model of §5.2.4.

5.4. Bit-mask Summary

Table 2 lists all mask bits included in the WSSA tiles of our data release. Throughout §5, bits 0-6, 8-13 have been explained. Bit 14 flags pixels that are saturated ($>30,000$ DN), but not marked as suspect by any of the msk file static mask bits. This can be useful downstream in identifying regions of extremely bright nebulosity that have reached saturation. Bits 7, 15-18 are only defined at the co-add level and are explained in §6.5.

5.5. Smoothing and Rebinning

Before writing our processed L1b files, we smooth to $15''$ FWHM, trim the smoothed image to 1000×1000 , and bin down by a factor of two in each dimension. We write the outputs of our L1b processing pipeline as multi-extension FITS files. For each raw L1b file in the All-Sky Release we write a corresponding processed file. The primary extension is the fully “cleaned” image, where we have removed point sources and their artifacts and SSOs. Extension 1 is the “dirty” image, which is merely a smoothed and rebinned version of the raw L1b image after interpolating as described in §5.1. Extension 2 is our bit-mask of §5.4, after dilation and rebinning that mimics the smoothing and rebinning of the first two extensions. These processed L1b images are not included in our data release, but will be made available upon request.

6. STACKING

We chose to co-add our processed L1b images on astrometric footprints analogous to those of the *IRAS* Sky Survey Atlas (ISSA) tiles (Wheelock et al. 1994). We

define a set of “WSSA” astrometric footprints with the same central (α, δ) values and same orientations relative to north as the original ISSA tiles, but precessed to J2000. As a result, each of our WSSA tiles does not identically cover the same region of the sky as its ISSA counterpart. Also, to accommodate our $15''$ FWHM, WSSA tiles have a pixel scale of $5.625''/\text{pixel}$, as opposed to $1.5''/\text{pixel}$ for ISSA tiles. There are 430 such $12.5^\circ \times 12.5^\circ$ WSSA tiles, with centers tracing out a series of isolatitude rings in J2000 equatorial coordinates. These tiles are not mutually exclusive; over the full sky, the median tile coverage is 1, but the mean coverage is 1.6, with a maximum of 5.

Our basic strategy in producing each WSSA tile is to start from the tile’s center and build outward, matching each image with the existing stack via a single offset before adding it in. Admittedly, this is a simple-minded approximate solution to the matrix inversion problem posed by best matching overlaps between neighboring exposures. In order to ensure that our simplistic procedure is feasible, we take two additional steps before beginning the stacking process, described in the following two subsections.

6.1. Gradient Correction

Overlapping L1b images may differ by more than a simple relative offset. This is especially true in regions that were imaged six months apart with opposite scan directions or near the ecliptic poles. In such cases, the zodiacal light can differ substantially between epochs. Even though the zodiacal light at a given epoch generally varies on spatial scales larger than a degree, this foreground is so strong that its gradient is readily apparent in single L1b exposures. As such, to ensure that our stacking can match neighboring exposures with a single offset, it is important to compute a correction for each exposure that removes time-dependent first order structure.

To arrive at such a gradient correction, we compare each L1b exposure to SFD $100\mu\text{m}$ on the same footprint. For each cleaned L1b exposure, we interpolate generously over bright source artifacts using our masks, then smooth to $6.1'$ FWHM to match i100 resolution and bin down $5\times$ in each dimension. We denote each pixel with coordinate x_i, y_i in this smoothed, rebinned $W3$ image as w_i . We then fit the following model to w_i :

$$w_i = f_{wi}i_i + \nabla_x x_i + \nabla_y y_i + C \quad (2)$$

Where f_{wi} , ∇_x , ∇_y , and C are the scalar parameters to be fit and i_i are the i100 values corresponding to w_i . The fit is performed via unweighted linear least squares, with iterative outlier rejection. ∇_x, ∇_y then specify x, y gradients that make the processed L1b exposure most consistent with Galactic emission, free of slowly varying time-dependent foregrounds. f_{wi} is a factor that allows small-scale dust structure to be nulled, accounting for the fact that conversion factor between $W3$ and i100 will be different for different L1b pointings. Similarly, C absorbs any constant offset arising from the WISE and i100 zero points. Our model for the time-dependent gradient in each exposure is computed from ∇_x, ∇_y , and subtracted before the mosaicking process begins. We only desire the gradient terms, and make no use of f_{wi}, C downstream.

6.2. Pairwise Rejection

Despite our metadata cuts (§2.3), some L1b images with severe systematic problems remain and could potentially corrupt the stacking process if allowed to contribute to our co-adds. To remove such images, we employ a pairwise comparison between overlapping L1b exposures.

Specifically, each gradient-corrected, processed L1b image is compared to up to 20 of its nearest neighbors at the locations of $N_{\text{side}} = 2048$ HEALPix pixel centers on which the frames overlap. For each pair, we compute the RMS of the differences between the sampled values. Then, for each image, we compute the median of these RMS values, \mathcal{R}_{med} . We then reject the highest \mathcal{R}_{med} frame with $\mathcal{R}_{\text{med}} > 500$ DN, updating \mathcal{R}_{med} for all other frames after each rejection, until no frames remain with $\mathcal{R}_{\text{med}} > 500$ DN. $\sim 0.4\%$ of images are rejected by the pairwise comparison, but these frames would have inflicted a disproportionate, negative influence on our stacks given the severity of their systematic problems.

6.3. Initial Stack

For each WSSA tile, we co-add the constituent L1b exposures onto the relevant astrometric footprint, with pixel scale of $5.625''/\text{pixel}$. $12.5^\circ \times 12.5^\circ$ co-adds are thus 8,000 pixels on a side. Such tiles are well-sampled because we have smoothed our processed L1b images to $15''$ FWHM.

We obtain a list of L1b exposures that will overlap the tile’s astrometric footprint, sorted by proximity to the tile center. We apply the gradients of section §6.1 to each cleaned L1b image, and then use the pairwise rejection step to reject the typically small number of problematic exposures. Starting with the exposure closest to the center, we add the cleaned L1b exposures into the stack one at a time, applying a single offset to make each exposure best agree with the existing stack. This offset is simply the median value of the difference between the exposure at hand and the existing stack on their overlap. As we stack, we also keep track of the minimum and maximum single-exposure pixel values at each pixel in the co-add footprint. We also store an integer coverage map, incrementing the relevant pixels each time an L1b image is added to the stack. For locations in the completed co-add that have coverage >2 , we subtract out the average of the minimum and maximum images at those locations, and adjust the coverage map appropriately. We will refer to the average of the minimum and maximum images as the “transient artifact image”. This outlier rejection step eliminates satellite streaks and any other unusual single-epoch features not specifically addressed by our L1b processing pipeline. We also apply the per-frame offsets to the dirty extension of our L1b images to create a corresponding stack with all point sources, bright source defects, and SSOs present.

6.4. Reference Comparison

With our initial WSSA tile stacks in hand, we can perform some further refinements, using the existing stack as a reference. There are two typically low-level problems we address by making use of our reference stack: (1) per-quadrant polynomial offsets in individual L1b exposures and (2) striping artifacts in L1b images.

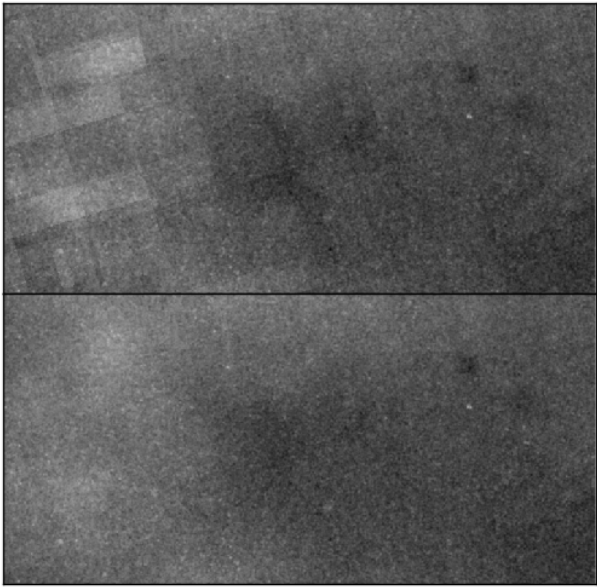


FIG. 7.— $1.2^\circ \times 0.6^\circ$ region within WSSA tile 221, at $(l, b) \approx (5^\circ, 48^\circ)$. Top: before reference warping. Bottom: after reference warping, with jagged L1b exposure boundaries eliminated.

6.4.1. Per-quadrant Polynomial Warps

We have already addressed scalar intensity offsets and gradient corrections on a per-exposure basis. But within a given exposure, the four quadrants can be offset relative to each other due to four-amplifier detector readout. These offsets can be simple scalars, but in some cases involve higher order polynomials (e.g. a gradient across one quadrant that is absent in the other quadrants). We refer to these polynomial offsets as per-quadrant “warps”. For fixed position on the celestial sphere within our co-adds, such warps in the various contributing L1b quadrants are not correlated. As such, any warping will be suppressed by $\gtrsim 90\%$ in our initial stacks.

Thus, we may reasonably consider our initial stacks to be nearly free from the effect of such per-quadrant warping, and as a result use them as reference templates to correct individual L1b quadrants. Doing so can help eliminate any jagged L1b quadrant edges that persist at low levels in the initial stacks. For each tile, we gather the same sample of L1b exposures as in §6.3. We then rebuild the mosaic from scratch, one L1b quadrant at a time, first fitting a per-quadrant warp relative to the reference, and then subtracting the warp model before adding the corrected quadrant into the revised stack.

Our warp model is simply a polynomial in the the relevant cleaned L1b quadrant’s x, y coordinates. For each such quadrant, we fit a fourth order polynomial to the difference between the cleaned L1b image and the reference stack. The fit is performed via unweighted linear least squares. With the best-fit polynomial computed, we evaluate the χ^2 goodness of fit between the reference stack and the corrected L1b quadrant. We take the expected pixel variance in each pixel of the cleaned L1b image to be:

$$\sigma_i^2 = f_s^2(R^2 + \frac{N_i}{g}) + (\delta g N_i)^2 + (\nabla N|_i \delta_\theta)^2 \quad (3)$$

Where N_i is the cleaned L1b pixel value in DN, $R =$

16.94 DN is the readnoise, $g = 6.83 e^-/\text{DN}$ is the gain, f_s is a constant that accounts for our smoothing/rebinning, δg is an estimate of the fractional gain variation, $\nabla N|_i$ is the magnitude of the reference image gradient evaluated at pixel i , and δ_θ is an estimate of the L1b astrometric error. N_i is floored at zero in the second term, since it is possible that e.g. a bright source residual could have negative values. $\nabla N|_i$ is calculated based on the reference stack, not the L1b image being compared to the stack. Based on studies of point sources presented in Cutri et al. (2012), we chose $\delta g = 0.025$ and $\delta_\theta = 0.4''$. The first two terms account for statistical errors in the cleaned L1b image. The second term allows for the possibility that the per-quadrant L1b gain may vary slightly. The final term accounts for astrometric imperfections that could cause the L1b exposure to be out of alignment with the reference stack. We assume that statistical errors in the reference stack are negligible relative to those in the L1b quadrant of interest.

If the $\chi^2/\text{D.O.F.}$ is greater than 7 for a particular L1b quadrant after applying the best-fit polynomial warp, that quadrant is excluded from the stack. 2% of L1b quadrants were thus rejected. Figure 7 shows a region in which L1b boundaries in the initial stack of §6.3 are corrected by our quadrant warping procedure.

6.4.2. Destriping

L1b exposures display low-level striping. Complicating matters, this striping occurs with different amplitudes and on different wave numbers from exposure to exposure, and even from quadrant to quadrant within single exposures. Still, a particular set of relatively few modes tend to be enhanced, as the stripes within a given quadrant are typically oriented parallel to the scan direction and have wavelengths of $\sim 2.5' - 4'$. To avoid high-pass filtering diffuse structure, our destriping never modifies modes larger than $4.6'$. We assume the striping to be an additive rather than multiplicative defect.

As such, our first step towards correcting L1b striping is to make a mask in Fourier space of the typically contaminated modes, using $\sim 20,000$ cleaned L1b images at very high $|b|$, where there are few compact sources and diffuse structure is minimal. For each of these L1b exposures, we compute the isotropic Fourier power spectrum in each quadrant. We label any mode “contaminated” which has a modulus-squared that is a $>5\sigma$ outlier relative to the appropriate isotropic value. We construct a mask of frequently contaminated modes by counting the number of occurrences of such outliers at each pixel within the quadrant FFT.

For each quadrant that successfully passes the quadrant warping step of §6.4.1, we attempt a destriping correction before finally adding the quadrant into the reference-corrected stack. We take the FFT of the quadrant under consideration and identify any $>5\sigma$ outliers relative to the isotropic power spectrum. We then modify the FFT values of those outliers which coincide with modes we previously flagged as frequently contaminated. We rescale such outliers to have a modulus that matches the appropriate isotropic value, leaving the phase unchanged. Transforming back to the spatial domain yields a destriped image.

For most L1b quadrants, this correction removes all apparent striping artifacts. However, there are cases in

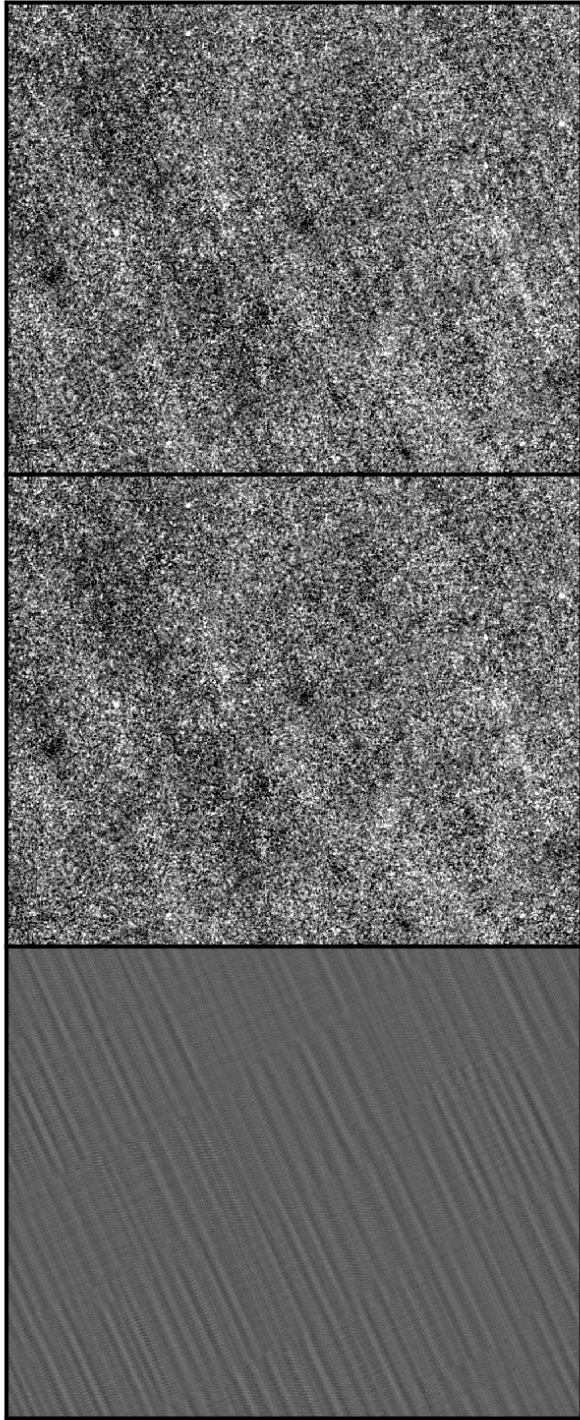


FIG. 8.— $1.6^\circ \times 1.3^\circ$ sub-region within WSSA tile 339, at $(l, b) \approx (188.7^\circ, 56.2^\circ)$. Top: before destriping. Middle: after destriping. Bottom: stripe model. The stripes are parallel to the scan direction.

which the correction can go awry. For example, the residuals of bright source artifacts can be aligned with the scan direction, wreaking havoc with our analysis meant to deal with low-level striping of the same orientation. We therefore incorporated destriping into our reference comparison process, in order to robustly identify such problematic instances. Specifically, we perform a chi-

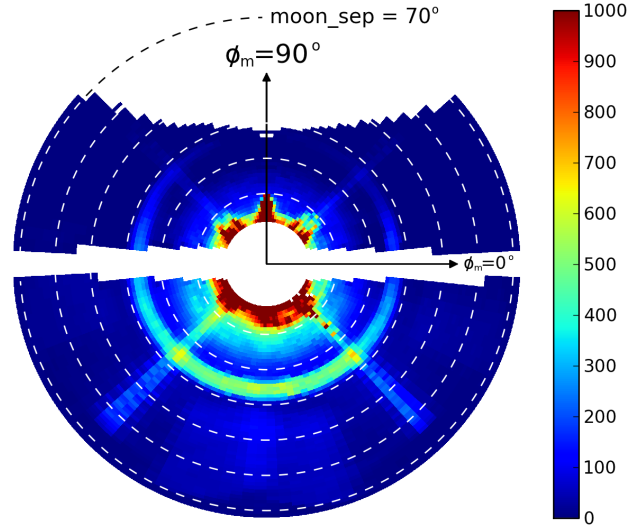


FIG. 9.— Our model for *W3* off-axis Moon-glow as a function of angular separation `moon_sep` (radial coordinate) and position angle ϕ_m (azimuthal coordinate). The units are *W3* DN, and dashed white circles denote intervals of 10° in `moon_sep`. Diffraction spikes are apparent out to `moon_sep` $> 60^\circ$. $0^\circ < \phi_m < 180^\circ$ tends to correspond to lower Moon phase than $-180^\circ < \phi_m < 0^\circ$, and is thus fainter.

squared comparison between each L1b quadrant and the reference stack, both before and after destriping. We use the pixel variances of §6.4.1. We then apply the destriping correction only if (1) the destriping correction improves the $\chi^2/\text{D.O.F}$ and (2) more individual pixels within the quadrant have their χ^2 improved than worsened by destriping. Since the striping is most apparent in regions of very low signal/background, and the destriping correction is very successful in such regions, we find this “do no harm” approach to be satisfactory. Figure 8 shows an example of our destriping correction.

6.5. Mosaic-Level Mask Bits

The following subsections describe mask bits defined at the mosaic level, rather than the L1b level.

6.5.1. Moon Mask

While our metadata cuts remove L1b frames pointed near the Moon (`moon_sep` $\leq 12^\circ$), off-axis Moon-glow can adversely affect exposures with much larger `moon_sep` values. In fact, prominent off-axis Moon illumination features extend out to many tens of degrees away from the Moon’s location. Accounting for the WISE survey strategy, this illumination detrimentally contaminates a non-negligible fraction, $\sim 5\text{--}10\%$, of the sky. Adverse effects on our stacks arise because the extended Moon-glow violates our assumption that the differences between exposures can be accounted for by an offset and linear gradients. For example, Moon-glow diffraction spikes can imprint strong, higher-order structure within a single L1b frame (see Cutri et al. 2012, §2.4b).

We derived an empirical model of *W3* off-axis Moon illumination in order to flag portions of our stacks which suffer serious Moon-glow corruption. In ecliptic coordinates, Moon-contaminated regions trace out a series of narrow vertical bands, a few degrees wide and generally separated by $\sim 30^\circ$ in λ . We did not attempt to

characterize sub-exposure Moon-glow structure, but instead created a model of the additive offset to the WISE zero point due to Moon illumination. Our model is not a function of (λ, β) , but rather Moon angular separation (`moon_sep`) and Moon position angle relative to the WISE optics (termed `$\phi_m = \text{moonpa} - \text{w3pa}$`). To arrive at such a model, we generated a full-sky $W3$ map, taking the L1b zero point at face value. We then subtracted $1.2\times$ the Kelsall model to roughly cancel the zodiacal light. Next, we smoothed to $6.1'$, and subtracted scaled SFD i100 assuming $\text{i100}/W3 = 17.5$, to approximately cancel diffuse Galactic emission. We designated particular, narrow ranges of λ as Moon-affected, and created a Moon-free prediction by interpolating over such regions at constant β . Restricting to $|b| > 15^\circ$, the difference between the Moon-free prediction and the corresponding L1b data constitutes our Moon-glow estimate, which yields the profile shown in Figure 9 when binned in (`moon_sep`, `ϕ_m`). We also created analogous profiles in Moon phase and Moon distance to enable corrections for these factors when predicting Moon contamination for individual L1b pointings.

As we stack, at each pixel in the co-add, we keep an integer count of the number of Moon-affected frames contributing to that pixel. We define Moon-affected frames to be those for which our model predicts moon contamination of $S_m > 100$ DN, and $S_m/\mathcal{R}_{100} > 450$. Pixels with Moon-contamination count > 3 at the end of the stacking process are flagged with bit 15, as listed in Table 2.

In rare cases typically associated with moon contamination, all L1b quadrants at a particular sky location are rejected during the reference comparison step. Mask bit 19 labels such locations, at which we have tapered in the reference stack to avoid leaving regions of missing data in the final mosaic. 0.15% of the sky is affected.

6.5.2. Resolved Compact Sources

Though we have carefully removed pointlike sources, there are many resolved compact sources in the WISE All-Sky Catalog. These objects, which include galaxies and multiple sources, do not belong in our map of diffuse Galactic cirrus. Instead of attempting to model and subtract such sources, we have simply added mask bit 7 to flag their locations, allowing users to ignore or interpolate over the affected regions.

To obtain a catalog of resolved, compact $W3$ sources, we cross-matched WISE All-Sky Catalog objects with `w3snr` > 2 , `ext_flg` = 5 to 2MASS XSC sources, with a matching radius of $5''$. We excluded XSC objects with `cc_flag` = a or `cc_flag` = z, and additionally discarded the 3712 XSC sources believed to be fragments of diffuse Milky Way dust (Skrutskie et al. 2006, §2.3b). This resulted in a list of $\sim 150,000$ resolved $W3$ sources. In order to obtain the best possible set of attributes for each such object, including the semi-major axis to semi-minor axis ratio r_{ab} and position angle θ_{PA} , we cross-matched our resolved $W3$ source list to the PGC catalog (Paturel et al. 2003), with a matching radius of $1'$.

We proceed to merge attributes from the XSC and PGC catalogs. We assign PGC values for r_{ab} and θ_{PA} to all PGC-matched sources with both values available in the PGC catalog. For objects with PGC major axis $> 1'$, but lacking either r_{ab} or θ_{PA} in the PGC catalog, r_{ab} and θ_{PA} are assigned to their XSC values. All other sources

are assigned a default value of $r_{ab} = 1$. Relatively large sources with PGC major axis $> 1'$ are assigned their respective PGC major axis value. All other sources are assigned a major axis of $1'$. To be conservative and avoid overly line-like masked regions, we cap r_{ab} at 2. The LMC, SMC, and M31 are excluded from the bit 7 mask and flagged separately (see §6.6.1).

For each WSSA tile, we then create a resolved object mask by flagging elliptical regions corresponding to the relevant entries from our WISE/XSC/PGC catalog. Over the entire sky, only 0.07% of pixels are thus flagged.

Our cross-matching procedure may occasionally discard true $W3$ sources in cases of exotic morphology (e.g. Barnard’s Galaxy), or in the event of a WISE All-Sky Catalog or XSC failure. To be conservative, we created mask bit 16, which uses the available PGC parameters of any prominent optical galaxies missing from our cross-match to again flag appropriate elliptical regions. To isolate such a sample of ‘prominent’ optical sources, we restricted to the subset of PGC sources with an RC3 counterpart (Corwin et al. 1994). Before generating this mask, we carefully excluded 18 large ($> 5'$ diameter), dIrr or dSph galaxies which are completely invisible in $W3$ (e.g. the Fornax Dwarf). In all, bit 16 masks only 0.005% of the sky.

6.6. Low Integer Frame Coverage

In regions with low integer frame coverage < 5 , compact sources are listed only in the WISE All-sky Reject Table, and are excluded from the All-sky Source Catalog (Cutri et al. 2012). Rather than attempt to identify valid sources among Reject Table entries, we opted instead to flag such regions with mask bit 21. 1.2% of the sky is affected.

6.6.1. Big Objects

The SFD mask contains a so-called “big object” bit, which labels regions affected by extragalactic sources with exceptionally large apparent sizes: the LMC, SMC, and M31. Bit 17 of our masks is meant to flag these same three objects. Our big object mask is identical to that of SFD for the irregularly shaped LMC and SMC. For M31, we use an ellipse based on PGC catalog parameters.

6.6.2. Low Ecliptic Latitude

Unfortunately, certain low ecliptic latitude regions were only observed by WISE while obstructed from view by a planet within our Solar System. In such cases, the planet appears as an extraordinarily bright, compact source and renders measurement of diffuse Galactic emission in its vicinity completely hopeless. As a result, we have flagged circular regions about the centroid of each planet imprint, typically several degrees in diameter. We have also added mask bit 22 to flag all pixels immediately within the ecliptic plane, as these should generally be handled with extra caution. The approximate range of ecliptic latitudes flagged is $-2^\circ < \beta < 2^\circ$. Additionally, at low ecliptic latitude, we have noticed unexpected line-like features $\sim 5.5'$ wide and extending many degrees in length. The origin of these lines is not known, and they do not appear to follow trajectories obviously indicative of an instrumental or processing malfunction, e.g. constant δ or constant β . Mask bit 20 marks the locations of such lines, which affect less than 0.15% of the sky.

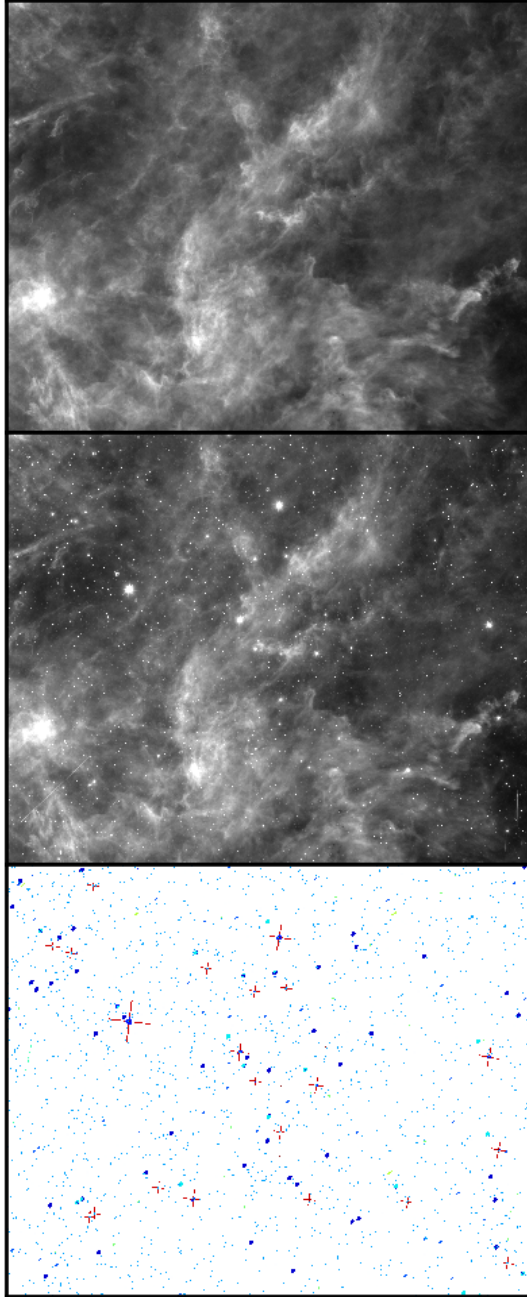


FIG. 10.— $4.3^\circ \times 3.8^\circ$ sub-region of WSSA tile 51, at $(l, b) \approx (266^\circ, -6^\circ)$, illustrating three of the extensions included in each of our tiles. Top: primary extension, diffuse Galactic $W3$ emission. Middle: ‘dirty’ extension, including point sources, satellite streaks, and SSOs. Bottom: colorscale rendering of ‘OR mask’ extension. Red crosses denote point source diffraction spikes.

7. FINAL WSSA TILES

In the following subsections we outline the final steps taken to convert our WSSA co-adds of §6 into the data products we have released.

7.1. Zero Point

Our mosaicking process only attempts to create a smooth image over each tile footprint by best matching each L1b exposure with its neighbors. However, this process does not ensure that neighboring tiles agree on

their overlaps. Further, relics of the zodiacal light and Moon contamination that aren’t perfectly removed by our SFD-based gradient correction can persist, leading to wandering of the tile zero points on relatively large scales of several degrees.

We investigated the possibility of obtaining a zero point by taking the L1b zero point at face value, and then subtracting out models for the time-dependent foregrounds. Despite our best efforts to subtract the Moon-glow model of §6.5.1 and various customizations of the Kelsall zodiacal light model (Kelsall et al. 1998), such an approach ultimately yielded a cosmetically unappealing result. Based on the Planck comparison we describe below, we estimate that, at high $|b|$, the true $W3$ Galactic emission is $\sim 0.5\%$ as bright as the $|\beta| = 90^\circ$ zodiacal light. While the Kelsall model appeared reasonable at the several percent level, this remained inadequate due to the overwhelming brightness of the zodiacal light at $12\mu\text{m}$.

We therefore resorted a zero point based on Planck (Planck Collaboration et al. 2013a). Henceforth, the term Planck will refer to Planck 857 GHz ($350\mu\text{m}$), corrected for zodiacal emission according to Planck Collaboration et al. (2013c). To ensure this Planck map contained only diffuse Galactic emission, we also interpolated over the SFD compact source mask. The great advantage of Planck relative to other full-sky, mid-IR and far-IR datasets is the very faint zodiacal foreground. The basic strategy will be to replace modes on scales of several degrees in our WISE tiles with appropriately rescaled and smoothed Planck.

In order to accomplish this goal, we must derive a map of the spatially varying coefficient f_{pw} that converts $350\mu\text{m}$ emission to $12\mu\text{m}$ emission. To derive f_{pw} we correlate cleaned WISE with Planck on a bandpass between $4'$ and $15'$. We break each tile into many $0.5^\circ \times 0.5^\circ$ rectangular patches and perform a linear least squares fit to the bandpass filtered WISE sub-image, where the model is bandpass Planck multiplied by f_{pw} , plus a constant offset. For each such fit, we also compute the Pearson correlation coefficient c of bandpass WISE versus bandpass Planck. We perform such fits over the full sky. For a variety of reasons, including poor signal to noise in Planck or WISE, or systematic issues in in Planck or WISE, c is often closer to zero than to unity. In such cases, the fit is driven to $f_{pw} \rightarrow 0$ for reasons that are instrumental rather than astrophysical. In order to obtain a map of f_{pw} on large scales, we make a cut on $c > 0.7$ and smooth the map of f_{pw} at those locations to 15° . With WISE in $W3$ DN and Planck in MJy/sr f_{pw} , varies between 2.2 and 5.8. Converting WISE to MJy/sr according to Cutri et al. (2012) so that both data sets have the same units, this translates to $0.036 < f_{pw} < 0.095$.

To replace the large scale modes of WISE with those of Planck, we apply a $12.5'$ median filter to both data sets, and then smooth both to 2° . We inpainted over regions with strong molecular emission, defined as Planck Type 3 CO > 15 K km/s (Planck Collaboration et al. 2013b). We subtract 2° WISE from each tile, and then add in smoothed Planck, multiplied by f_{pw} . In order to derive tiles free of edge effects from the smoothing process, we initially built our WSSA stacks on $14^\circ \times 14^\circ$ padded astrometric footprints.

Lastly, we convert the WISE tiles with Planck-based

TABLE 3
WSSA TILE EXTENSIONS

| Extension | Description |
|-----------|--------------------------|
| 0 | cleaned co-add |
| 1 | dirty co-add |
| 2 | integer coverage |
| 3 | minimum value image |
| 4 | maximum value image |
| 5 | AND bit-mask |
| 6 | OR bit-mask |
| 7 | transient artifact image |

zero point from *W3* DN to MJy/sr according to the prescription of Cutri et al. (2012), §4.4h.

7.2. Tile Format

We release the 430 *W3* WSSA tiles as multi-extension FITS files. Table 3 lists the extensions included. Refer to the tile headers for further details.

8. DISCUSSION AND CONCLUSION

We have described and released⁵ a full-sky, 15'' resolution map of diffuse Galactic 12 μ m emission based on WISE images. Indeed, WISE *W3* provides valuable and striking small angular scale detail regarding the spatial structure of the ISM over much of the sky. We strongly encourage all interested astronomers to sample values from our mosaics, and also visually inspect the co-adds. We anticipate this to be the first in a series of papers, throughout which we demonstrate that an enhanced-resolution dust map based on WISE *W3* better predicts extinction than does SFD, and ultimately release such a full-sky data product for accessing improved reddening estimates.

Figure 11 shows the 12 μ m map we have derived, binned to 7' resolution. On large scales, the map looks very similar to the Planck 350 μ m data from which we derived our 12 μ m zero-point. The notable exceptions are stripes of moon contamination, which dominate our map over ~5% of the sky.

We conclude by briefly pointing out aspects of the WISE All-sky release processing that turned out to be suboptimal for the purpose of mapping diffuse emission, and finally compare our 12 μ m map to those of DIRBE and *IRAS*.

8.1. All-sky Release Processing

The “dynamic calibration sky offset correction” (Cutri et al. 2012, §4.4a) introduced several problematic features into the L1b frames which we did not address for this initial 12 μ m tile release. In particular, long-term latents due to bright sources are mirrored in acausal fashion to affect frames temporally *preceding* bright source detection. Examples of such features can be seen in Figure 8 as low-level, dark ‘divots’ ~1-2' in size. These acausal latents are the dominant remaining imperfection in many regions of our co-adds with low dust signal. In a related problem, the dynamic sky offset procedure can often assign up to ~4% of pixels in a given L1b image to exactly the median pixel value within the frame. Because

these issues would be better addressed with lower-level data products than the L1b images, we have so far opted not to address them.

8.2. DIRBE & IRAS Comparison

The relevant DIRBE data product to compare with our *W3* map is the band 5 “Zodi-Subtracted Mission Average” (ZSMA5). Because DIRBE pointed at a variety of Solar elongations, including some <90°, the DIRBE-observed zodiacal light is even more pronounced and complex than that in *W3*. Arguably, the most prominent feature in ZSMA5 is the *residual* zodiacal light left over after subtracting the DSZA model. The ecliptic plane is obvious in such residuals, and at high $|b|$ there remains a clear gradient of average flux with β , with magnitude of $\sim 6 \times 10^{-3}$ (MJy/sr)/deg, or ~ 0.2 MJy/sr between $|\beta| \sim 60^\circ$ and $|\beta| \sim 90^\circ$. By comparison, our Planck-based far-IR zero point suggests that at $|b| \gtrsim 80^\circ$, the *entire* non-IPD 12 μ m signal is ~ 0.03 MJy/sr. There is also a significant offset between ZSMA5 and our map in regions near the ecliptic poles, with amplitude ~ 0.6 MJy/sr. While it might be interesting to investigate these differences, they are immaterial to our long-term goal of predicting dust extinction. Thanks to our far-IR zero point, our *W3* map only shows traces of zodiacal light in rare circumstances, very near the ecliptic plane, where the zodi can vary strongly on scales smaller than 2°. Our *W3* map is also superior to ZSMA5 in that point sources remain un-subtracted in the latter, impacting a substantial fraction of the sky. On the other hand, DIRBE band 5 is truly a full-sky map, whereas ~5% of diffuse *W3* emission is badly contaminated by Moon-glow and/or Solar System planets.

IRAS 12 μ m has a separate “reject” data set at low $|\beta|$ that is not consistent with the remainder of their map. Thus, our *W3* map improves upon *IRAS* 12 μ m by virtue of (1) its consistent, zodi-free zero point (2) its factor of 16 enhancement in angular resolution and (3) our removal and masking of compact sources.

We thank Roc Cutri for his guidance in making use of the WISE data products. We also thank Bruce Draine for his careful reading of an early version of this manuscript.

We acknowledge support of NASA grant NNX12AE08G for this research. This research was conducted with Government support under and awarded by DoD, Air Force Office of Scientific Research, National Defense Science and Engineering Graduate (NDSEG) Fellowship, 32 CFR 168a. This research made use of the NASA Astrophysics Data System (ADS) and the IDL Astronomy User’s Library at Goddard.⁶

This publication makes use of data products from the Wide-field Infrared Survey Explorer, which is a joint project of the University of California, Los Angeles, and the Jet Propulsion Laboratory/California Institute of Technology, funded by the National Aeronautics and Space Administration. This publication also makes use of data products from NEOWISE, which is a project of the Jet Propulsion Laboratory/California Institute of Technology, funded by the Planetary Science Division of the National Aeronautics and Space Administration.

⁵ See <http://wise.skymaps.info>.

⁶ Available at <http://idlastro.gsfc.nasa.gov>

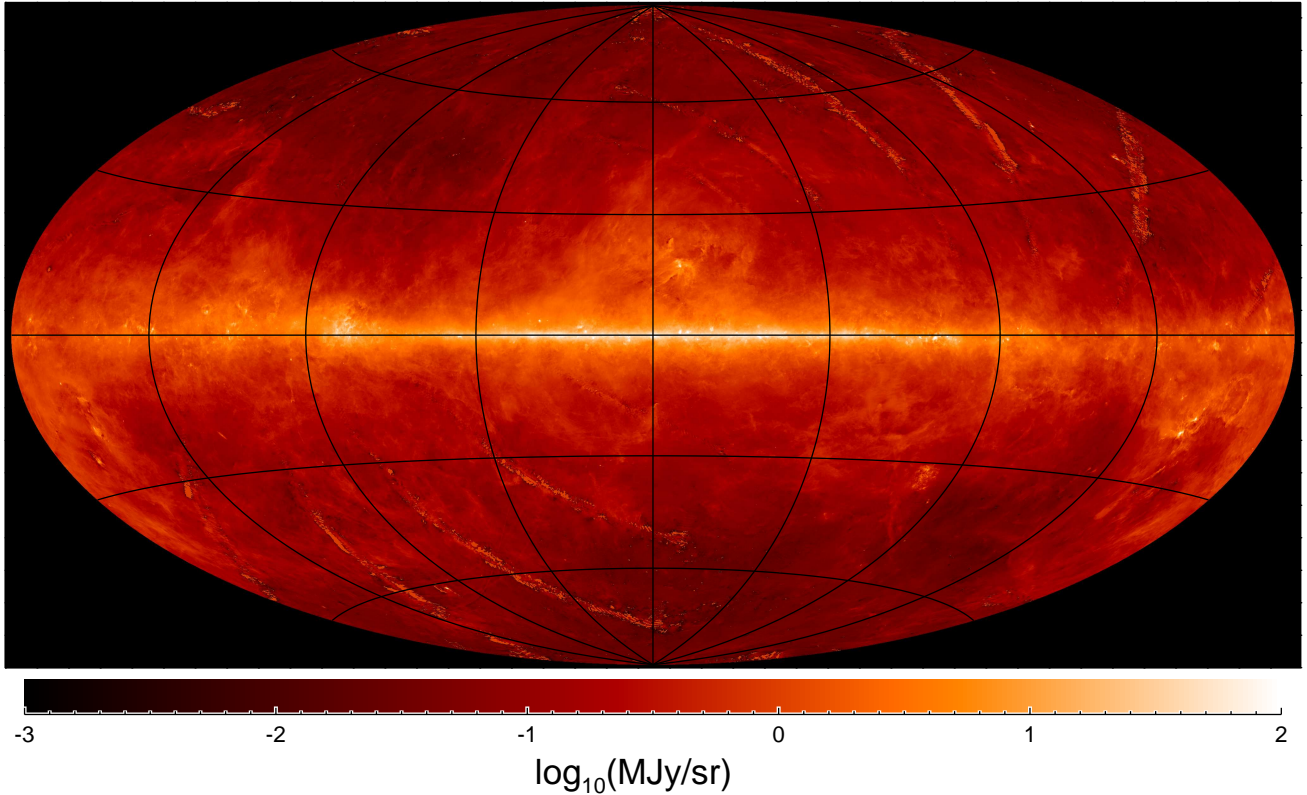


FIG. 11.— Our full-sky, 12 μ m map, binned to 7' resolution, in Hammer-Aitoff projection, on a logarithmic stretch.

This publication makes use of data products from the Two Micron All Sky Survey, which is a joint project of the University of Massachusetts and the Infrared Pro-

cessing and Analysis Center/California Institute of Technology, funded by the National Aeronautics and Space Administration and the National Science Foundation.

REFERENCES

- Boggess, N. W., Mather, J. C., Weiss, R., et al. 1992, *ApJ*, 397, 420
- Corwin, Jr., H. G., Buta, R. J., & de Vaucouleurs, G. 1994, *AJ*, 108, 2128
- Cutri, R. M., Wright, E. L., Conrow, T., et al. 2012, Explanatory Supplement to the WISE All-Sky Data Release Products, <http://wise2.ipac.caltech.edu/docs/release/allsky/expsup/>
- Górski, K. M., Hivon, E., Banday, A. J., et al. 2005, *ApJ*, 622, 759
- Kelsall, T., Weiland, J. L., Franz, B. A., et al. 1998, *ApJ*, 508, 44
- Kessler, M. F., Steinz, J. A., Anderegg, M. E., et al. 1996, *A&A*, 315, L27
- Low, F. J., Young, E., Beintema, D. A., et al. 1984, *ApJ*, 278, L19
- Mainzer, A., Bauer, J., Grav, T., et al. 2011, *ApJ*, 731, 53
- Onaka, T., Yamamura, I., Tanabe, T., Roellig, T. L., & Yuen, L. 1996, *PASJ*, 48, L59
- Paturel, G., Petit, C., Prugniel, P., et al. 2003, *A&A*, 412, 45
- Pilbratt, G. L., Riedinger, J. R., Passvogel, T., et al. 2010, *A&A*, 518, L1
- Planck Collaboration, Ade, P. A. R., Aghanim, N., et al. 2013a, arXiv:1303.5062
- . 2013b, arXiv:1303.5073
- . 2013c, arXiv:1303.5074
- Schlegel, D. J., Finkbeiner, D. P., & Davis, M. 1998, *ApJ*, 500, 525
- Skrutskie, M. F., Cutri, R. M., Stiening, R., et al. 2006, *AJ*, 131, 1163
- Tanaka, M., Matsumoto, T., Murakami, H., et al. 1996, *PASJ*, 48, L53
- Werner, M. W., Roellig, T. L., Low, F. J., et al. 2004, *ApJS*, 154, 1
- Wheelock, S. L., Gautier, T. N., Chillemi, J., et al. 1994, NASA STI/Recon Technical Report N, 95, 22539
- Wright, E. L., Eisenhardt, P. R. M., Mainzer, A. K., et al. 2010, *AJ*, 140, 1868